JACS Au
AN OPEN ACCESS JOURNAL OF THE AMERICAN CHEMICAL SOCIETY

pubs.acs.org/jacsau
Article

Venomous Peptides: Molecular Origin of the Toxicity of Snake Venom PLA_2-like Peptides

João T. S. Coimbra, Antoine Gissler, Emiel Nitor, Kiana Rostamipour, Ana V. Cunha, Maria J. Ramos, and Pedro A. Fernandes*

Cite This: JACS Au 2024, 4, 4295−4306
Read Online

ABSTRACT: Snakebite envenoming claims 81−138 thousand lives annually, with vipers responsible for many of those. Phospholipase A_2 (PLA_2) enzymes and PLA_2-like proteins are among the most important viper venom toxins. The latter are particularly intriguing, as three decades after their discovery, their molecular mechanism of toxicity is still poorly understood at best. PLA_2-like proteins destabilize eukaryotic cell membranes through an unknown mechanism, causing an uncontrolled influx of Ca^{2+} ions and ultimately triggering cell death. It is now clear that the C-terminal segment is fundamental to the toxicity, as 13-mer peptides with the same sequence exhibit most or all of the activities of the complete PLA_2-like proteins. To finally clarify the mechanism of toxicity of these venom peptides, we have simulated their interaction with model cell membranes. Molecular dynamics simulations showed that peptides initially dispersed across the cell membrane quickly and spontaneously migrated, aggregated, induced membrane thinning, and formed clear and transient membrane pores. We calculated the potentials of the mean force for Ca^{2+} transfer across the cell membranes through the transient pores. The pores significantly lower the free energy barrier for Ca^{2+} translocation, an effect that grows with the size of the peptide aggregates and, thus, with the pore radius. Ca^{2+} flowed across the membrane through the largest pores with almost no barrier. The permeability of Ca^{2+} through the largest pores exceeded the permeability of pharmaceutical drugs by 4 orders of magnitude, revealing the easiness by which Ca^{2+} overflows the intracellular medium. These results elucidate the illusive molecular origin of the toxicity of this famous class of snake venom-derived peptides.

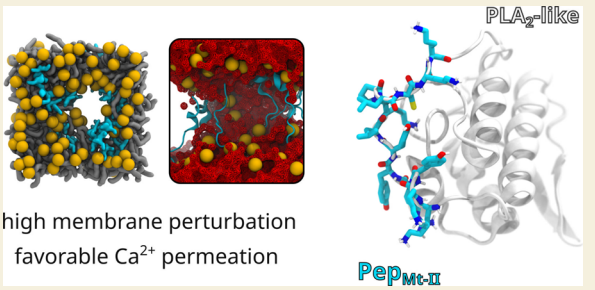

KEYWORDS: *snakebite envenoming, calcium, membrane active peptides, membrane pores, molecular dynamics*

INTRODUCTION

Snake envenoming is a neglected tropical disease that kills 81−138 thousand people and injuries more than 400,000 every year.[1,2] This disease shows high prevalence in Asia, Africa, and Latin America, especially in more rural populations due to isolation, lack of resources, and/or inaccessibility to adequate treatment.[1,2] Countries with less developed health systems and sparse medical resources show the highest burden of snakebites. Investment in antivenoms has also diminished, and prices have spiked in the last few decades, mainly due to low demand. This has prompted a World Health Organization (WHO) response, which listed snakebite envenoming as a highest-priority neglected tropical disease in June 2017 and inspired a strategy to reduce by 50% the mortality and disability caused by snakebites by 2030.[3]

The composition of snake venom shows high interspecific and intraspecific diversities,[2] resulting in a wide range of dramatic clinical manifestations, broadly divided into neurotoxicity, myotoxicity, and hemorrhagic activity. It is typically a very complex mixture with 20 to >100 components, over 90% of which are proteins and peptides.[2,4] Besides the large variations in venom composition between snake species, nongenetic effects, such as environmental conditions, age, sex, or type of prey, contribute to venom variability intraspecies.[2] The richness of the venom composition is a biodiversity treasure being used for drug discovery, with several drugs derived from snake venom already approved. At the same time, the venom diversity severely limits the efficiency of the treatment of snakebite victims, as it demands the administration of species-specific antivenoms.

Necrotic muscle damage is a common pathology associated with snakebites and a frequent cause of limb amputation, in particular in children.[1,2] That pathology is more common in viper envenomation and is mostly induced by the venom phospholipase A_2 (PLA_2) enzymes and proteins. It typically involves (i) hydrolysis of the skeletal muscle cell membrane phospholipids by PLA_2 enzymes, generating free fatty acids and

Received: July 17, 2024
Revised: September 19, 2024
Accepted: September 19, 2024
Published: October 22, 2024

https://doi.org/10.1021/jacsau.4c00646
JACS Au 2024, 4, 4295−4306

lysophospholipids, ultimately destabilizing the membrane's ion permeability and/or integrity—a well-documented effect[5−8]; additionally, the released fatty acids are metabolized into prostaglandins and leukotrienes, both of which play crucial roles in mediating inflammatory processes and pain[9]; and (ii) the action of PLA_2 proteins (also called PLA_2-like proteins),[10] which are nonenzymatic homologues of the more ancient of PLA_2 enzymes, whose mode of action is poorly understood, ultimately provoking membrane destabilization, skeletal muscle cell death, and muscle necrosis effects strikingly similar to their enzyme counterparts, despite being non-catalytic and acting through a completely different mechanism. Upon the action of those two toxins, cell death is initiated by a burst of intracellular calcium concentration caused by the damage the toxins do to the cell membrane.[6,11−14]

The Lys49 PLA_2-like proteins are the most abundant and studied class of PLA_2-like proteins, which have an active site Asp49Lys mutation (standard PLA_2 numbering)[15] that abolishes catalytic activity while still preserving the ability to cause cell necrosis as PLA_2 enzymes do.[16] Other less abundant groups have the Asp49 residue mutated by Ser, Arg, Asn, or Gln residues.[16]

In the 90s, Bruno Lomonte and co-workers identified the C-terminal segment (residues 115−129) as the key region for myotoxicity.[17,18] Later studies demonstrated that peptides with the 13-amino acid C-terminal sequence of the PLA_2-like proteins of several viper species preserve, partially or totally, the myotoxicity of the PLA_2-like proteins from which they were derived.[17,19] Further studies with the PLA_2-like derived peptides showed that they have strong anticancer, antimicrobial, and antiparasitic activity[2]; making them promising therapeutic agents, in particular against viruses and bacteria, as antimicrobial peptides (AMPs) are much less prone to resistance than conventional protein-targeting drugs.[20]

We studied here the PLA_2-like peptide taken from an important Lys49 PLA_2-like protein commonly known as Myotoxin-II (Mt-II, UniProtID: P24605), found in the venom of the large and very aggressive *Bothrops asper* pitviper (common name: terciopelo), a medically important snake and the leading cause of snakebite morbidity and mortality in its Central America and northern South American habitat (Figure 1).[21,22] This peptide (residues 115−129, KKYRYYLKPLCKK) was used as a representative of the viper venom PLA_2-like-derived peptide family. We investigated its mechanism of membrane destabilization and role in promoting the massive internalization of Ca^{2+} ions seen experimentally, which is the first phenomenon observed during cytotoxicity triggering.[16] We will refer to this peptide as $Pep_{Mt\text{-}II}$. Earlier studies have shown that this peptide is highly implicated in the myotoxicity activity of Myotoxin-II,[18] and the C-terminal region plays a vital role in toxicity.[23] The $Pep_{Mt\text{-}II}$ sequence contains two positive residues (Lys and/or Arg) at both termini and a core primarily composed of hydrophobic/aromatic residues interspersed with additional cationic residues. These structural features are crucial for membrane insertion and destabilization. Sequence alignments of the C-terminal region of PLA_2-like proteins from the venom of 58 viper species show that these characteristics are highly conserved. In contrast, they are absent in most PLA_2 enzymes that are myotoxic only via their catalytic activity.[24] An earlier molecular modeling study showed that the two positive residues match the negative phosphates of each leaflet very well when the peptide vertically inserts into the cell membrane parallel to the phospholipids.[25]

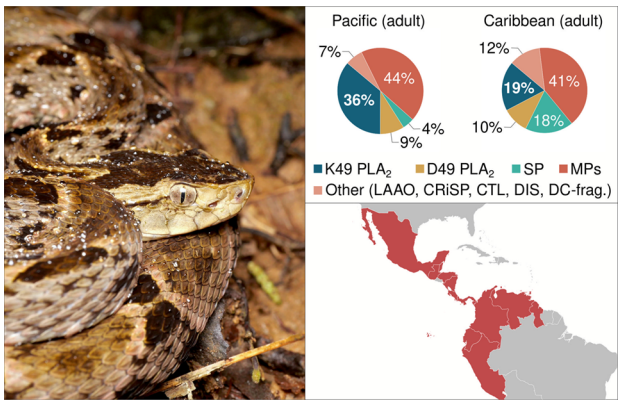

Figure 1. Overall protein composition of adult *B. asper* from the Caribbean and Pacific regions of Costa Rica and the countries where it has been observed (distribution may be confined to some regions in the highlighted countries). Venom composition is shown in percentage of the total HPLC-separated proteins. K49 PLA_2: Lys49 PLA_2-like protein family; D49 PLA_2: Asp49 PLA_2 protein family; SP: serine proteinase family; MPs: Zn^{2+}-metalloproteinase family; LAAO: L-amino acid oxidase family; CRiSP: cysteine-rich secretory protein family; CTL: C-type lectin-like family; DIS: medium-sized desintegrin family; DC-frag.: DC-fragments. Most venoms possess several enzymatic and proteic isoforms within a family. Reproduced from ref 21. Copyright 2008 American Chemical Society. The snake in the photograph was identified as *B. asper*. Reproduced from "Rauhschuppige lanzenotter, terciopelo, víbora equis" by Philipp Hoenle. The image is dedicated to the public domain under CC0 1.0.

However, the snake venom peptides have characteristics that we suspect are membrane-disruptive.[24] First, they have Lys or Arg residues at the central hydrophobic core of the peptides, which may provoke electrostatic destabilization in the membrane. Second, they hold several branched and aromatic side chains in the same region, which, despite being hydrophobic, may provoke steric destabilization in the membrane.

This observation prompted us to investigate the consequences of the vertical insertion of $Pep_{Mt\text{-}II}$ in model cell membranes of varied composition, as this might be a key to understanding the general mechanism of action for the peptides derived from PLA_2-like proteins. This vertical insertion resembles the mechanism of action of other structurally different AMPs, for which there is evidence that they insert into the lipid bilayer and create peptide-lined pores or peptide-and-lipid-lined pores, described by the barrel stave or toroidal pore models.[26,27] The eventual self-organization and formation of membrane pores by the peptides derived from snake venom align with the experimentally observed membrane leakage upon peptide exposure. Using coarse-grained (CG) and, mostly, all-atom (AA) molecular dynamics (MD) simulations, we inserted a growing concentration of $Pep_{Mt\text{-}II}$ into the cell membranes and calculated potentials of mean force for Ca^{2+} translocation. The results generated a new understanding of the puzzling molecular mechanism of cytotoxicity of the peptides derived from snake venom PLA_2-like proteins.

https://doi.org/10.1021/jacsau.4c00646
JACS Au 2024, 4, 4295−4306

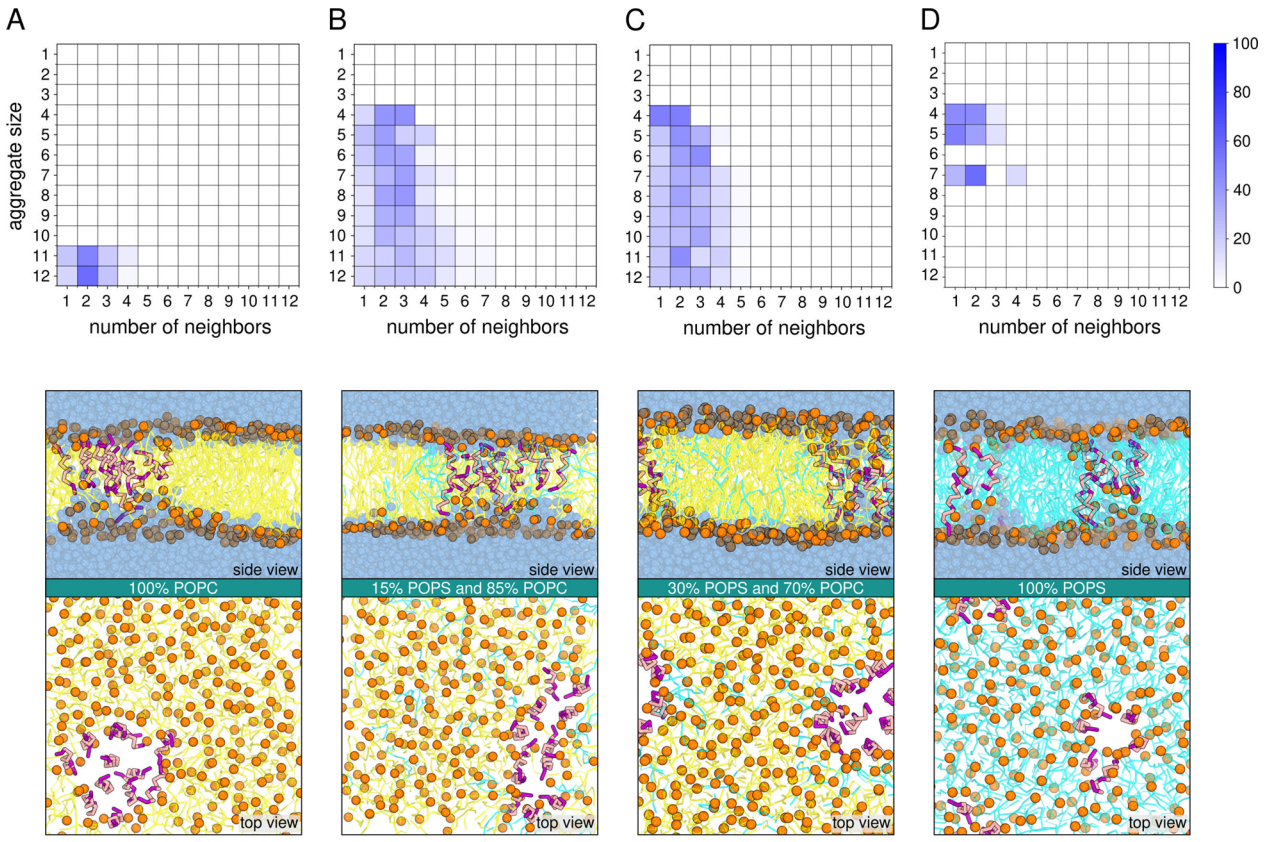

Figure 2. Top row: average probability of aggregate formation on membranes with different compositions. (A) 100% POPC; (B) 15% POPS and 85% POPC; (C) 30% POPS and 70% POPC; (D) 100% POPS. The probability is given in percentage, with colors ranging from white to blue—white corresponds to 0% and blue to 100%. Bottom row: side-view and top-view of the same four CG membrane-peptide-water systems. The peptides are highlighted as thick pink sticks (with Lys residues colored magenta), POPC phospholipids colored yellow, and POPS phospholipids in cyan. The phosphate groups are illustrated as orange spheres and water beads in blue (with transparency). For the top-view, water beads were omitted for clarity. The presented structures were generated from the last structure of the production CG MD simulation.

RESULTS AND DISCUSSION

Simulations of $Pep_{Mt\text{-}II}$ Aggregation Within a Cell Membrane Using Coarse-Grained Molecular Dynamics (CG MD)

Four distinct cell membrane compositions were examined: (i) 100% 1-palmitoyl-2-oleoyl-glycero-3-phosphocholine (POPC); (ii) 15% 1-palmitoyl-2-oleoyl-*sn*-glycero-3-phospho-L-serine (POPS) and 85% POPC; (iii) 30% POPS and 70% POPC; (iv) 100% POPS. This range of POPC/POPS concentrations mimics the microheterogeneity of the distribution of zwitterionic and negative phospholipids in a cell membrane and the progressive enrichment in negative fatty acids after snakebite envenomation due to the hydrolytic activity of PLA_2 enzymes (before envenomation, the average zwitterionic to negative phospholipid ratio in myotubes, the target of PLA_2-like proteins, is ca. 85% to 15%).[7] The analysis of peptide aggregation was done with the AGGREGATES software (Figure 2).[28]

We started the simulations in every membrane with monodispersed peptides to investigate whether they would spontaneously aggregate, which quickly happened in all cases. For the 100% POPC membrane, we found large aggregates of 11−12 peptides. The number of neighbors for each peptide differed within a range of 1−4, with higher probabilities for two neighbors (ca. 50%) and lower probabilities for four neighbors (ca. 3%). The top row of Figure 2 illustrates the results. This analysis determined the width and order of the peptide aggregate chains. In a perfect ring, each peptide has only two peptide neighbors, whereas in a more disordered, thicker aggregate, each peptide has a higher number of neighbors. We observed the latter type of disordered aggregates in the membrane with 85% POPC and 15% POPS—a broader distribution of aggregate sizes, ranging from 4 to 12 peptides, having more than two neighbors more often than in the pure POPC counterpart. We found a similar pattern at the membrane with 30% POPS and 70% POPC, although with a slightly higher probability of finding peptides with two neighbors, thus forming more ordered, circular aggregates. The aggregates in the 100% POPS membrane are smaller, ranging from 4 to 7 peptides, with aggregates of 4 peptides having equal probabilities for one or two neighbors (around 45%), whereas aggregates of 7 peptides showed higher probabilities of each peptide having two neighbors (ca. 57%). Therefore, larger aggregates are slightly more ordered than their smaller counterparts.

These results are supported by a visual inspection of the CG MD simulation (Figure 2). The side view representation of the 100% POPC membrane shows water beads penetrating the membrane and the phospholipid heads interacting with the Lys residues. This suggests that the charges of the POPC lipids may induce a stabilizing effect on the peptides, maintaining them in an aggregated state due to the electrostatic attraction between the lipidic heads and the residues. These results are

https://doi.org/10.1021/jacsau.4c00646
JACS Au 2024, 4, 4295−4306

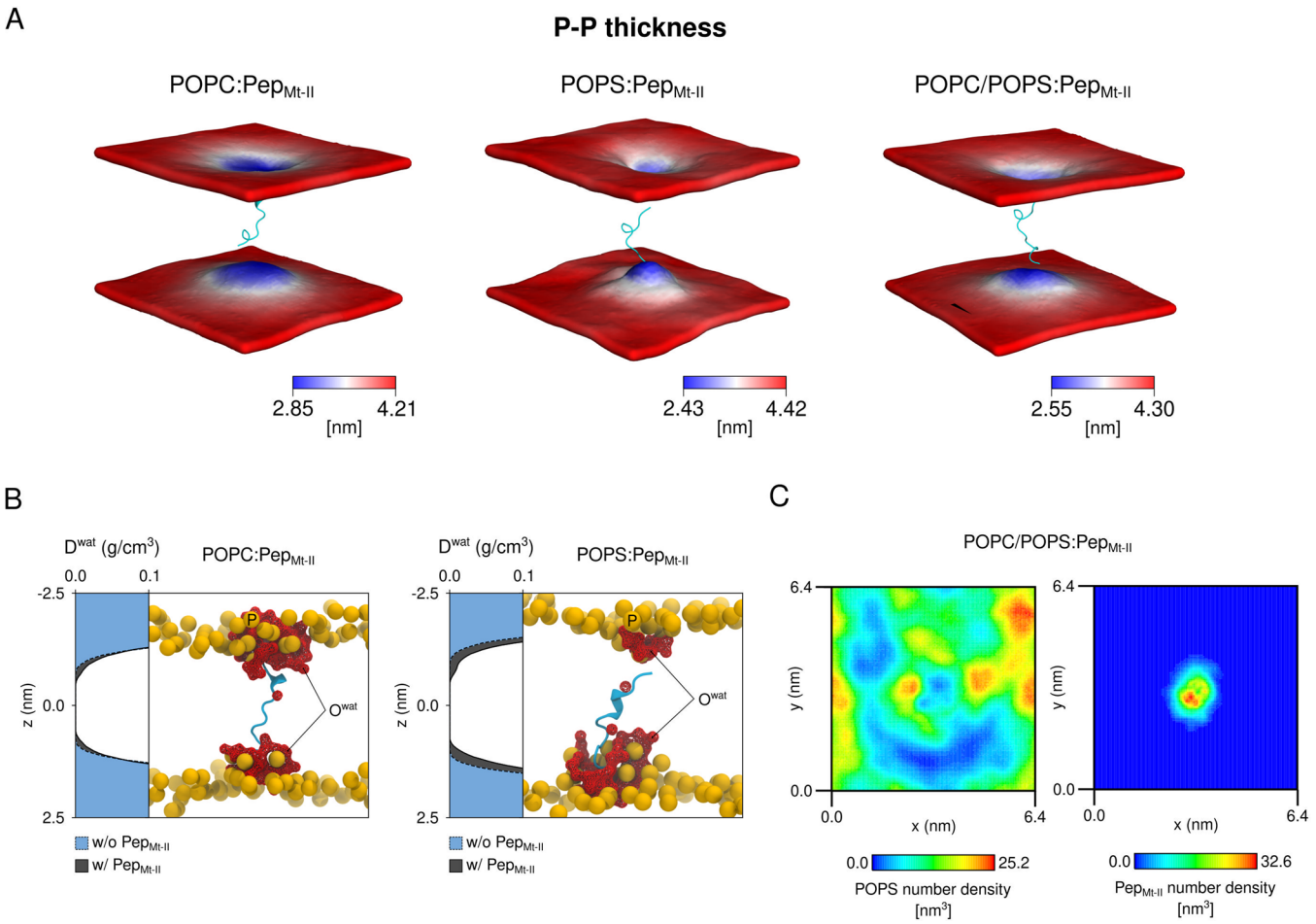

Figure 3. Local bilayer thickness, water insertion, and POPS/Pep$_{Mt-II}$ distribution in the bilayer plane (*xy*). (A) Time-averaged local bilayer thickness for systems with Pep$_{Mt-II}$ inserted in pure POPC and POPS membranes and in a 75% POPC and 25% POPS mixture. The analysis was performed considering the position of the P atoms (P−P thickness) of the lipid molecules. (B) Water molecules within 0.5 nm of Pep$_{Mt-II}$ at the end of the MD simulation (red mesh) and the P atoms (orange spheres). Pep$_{Mt-II}$ is shown in blue. All other water molecules, ions, and lipid atoms are omitted for clarity. The density of the water molecules along the bilayers' normal (dark gray) and for the equivalent bilayer systems without Pep$_{Mt-II}$ is in cyan. This analysis was performed considering the last 100 ns of simulation of each system. (C) POPS and Pep$_{Mt-II}$ number densities along the *xy* plane averaged over the last 100 ns of the simulation.

consistent with previous published studies in the literature in which the importance of charge interactions for aggregate formation and the effect of the amino acid charges on the pore type have been described.[29]

For the mixed phospholipid membranes (15% POPS and 85% POPC, and 30% POPS and 70% POPC), Pep$_{Mt-II}$ molecules are more dispersed when compared to the pure POPC counterpart (Figure 2), and the POPS phospholipids move toward the peptide aggregate, thereby surrounding them. This behavior likely causes a disruption of the Pep$_{Mt-II}$ aggregates and the formation of smaller size aggregates. At higher POPS concentrations (30 and 100% POPS), phospholipid head tilt is more pronounced than in the other situations. The POPS lipidic heads interact more with the Lys residues of the peptides (Figure 2). The dependence of the pore shape with the membrane composition agrees with earlier studies.[29]

In summary, CG MD simulations clearly show that the snake venom-derived Pep$_{Mt-II}$ initially spread through cell membranes of different local compositions, migrated through the membrane, and spontaneously formed aggregates in all cell membranes. The aggregates have varying sizes, order, and circularity, depending on the proportion of negative phospholipids. Having established this, we proceed to much more CPU-intensive Pep$_{Mt-II}$ membrane all-atom (AA) simulations to analyze the effect of the Pep$_{Mt-II}$ peptides on membrane thickness and order and to calculate potentials of mean force for Ca^{2+} internalization to determine if the observed aggregates are at the origin of the intense toxicity of the peptides. Given the very demanding nature of the all-atom calculations, we simulated a smaller number of peptide aggregates of different sizes.

All-Atom Simulations of the Impact of Pep$_{Mt-II}$ in the Structure of Cell Membranes

The snake venom-derived Pep$_{Mt-II}$ was inserted in three model cell membranes of different compositions—pure POPC, pure POPS, and a binary lipid system containing 75% POPC and 25% POPS. Earlier studies showed that the snake venom-derived peptides disrupted negatively charged vesicles far more efficiently than positively charged liposomes. Some liposome studies have employed molar ratios of negatively charged phospholipids ranging from 10% to 50%.[30]

First, we inserted a single Pep$_{Mt-II}$ in pure POPC and pure POPS membranes and observed, in both, a pronounced

https://doi.org/10.1021/jacsau.4c00646
JACS Au 2024, 4, 4295−4306

Table 1. Values for ΔG_{bar}, ΔG_{par}, and ΔG_{max} in kJ mol^{-1}, Extracted from the PMFs of Each Umbrella Sampling Simulation[a]

system	POPC/POPS/Pep$_{Mt-II}$	ΔG_{bar} (kJ/mol)	ΔG_{par} (kJ/mol)	ΔG_{max} (kJ/mol)	P_m (cm/s)
AA-1	128/0/0	101	−3	98	7.3×10^{-15}
AA-2	0/128/0	145	−25	120	7.0×10^{-18}
AA-3	128/0/1	77	−1	76	4.0×10^{-11}
AA-4	0/128/1	94	−29	65	6.7×10^{-9}
AA-7	96/32/5	60	−9	51	1.3×10^{-6}
AA-8	96/32/13	16	−3	13	8.9×10^{-1}
experiment[47]	eggPC, 37 °C				9.8×10^{-14}

[a]Membrane permeability results (P_m) for Ca^{2+} are in cm s^{-1}.

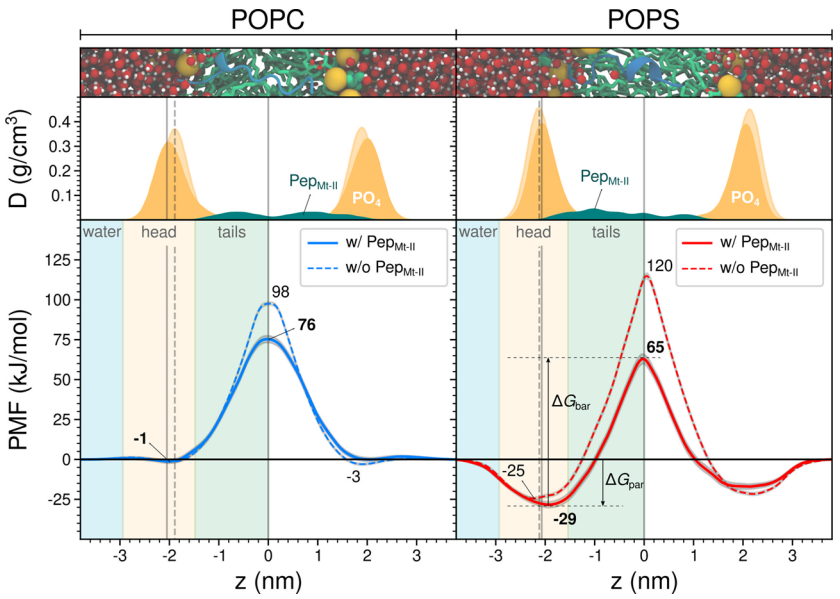

Figure 4. PMF profiles of Ca^{2+} translocation along membranes. (Top) Density of the phosphate groups in pure POPS and POPC bilayers, with (opaque) and without (transparent) a single Pep$_{Mt-II}$ molecule. The density of Pep$_{Mt-II}$ is also shown. (Bottom) PMFs for Ca^{2+} translocation through the membrane (dashed line) and close to the Pep$_{Mt-II}$ molecule (full line). The vertical gray lines mark the distance from the bilayer center of the average peak density of the phosphate groups of the phospholipids for each setting, i.e., with (full line) and without (dashed line) the peptide inserted. The minimum and maximum values of the PMFs are represented as well as an illustration of ΔG_{bar}, and ΔG_{par} in one of the panels.

membrane thinning around the peptide (Figure 3). Peptide-induced membrane thinning was also observed for other antimicrobial and membrane fusion peptides.[31−33] This effect was more substantial for the POPS membrane with a minimum P−P thickness of 2.43 nm, contrasting with a significantly larger minimum P−P thickness of 2.85 nm for pure POPC. Water molecules penetrated the hydrophobic region of the bilayer by establishing favorable interactions with polar groups of Pep$_{Mt-II}$ (Figure 3), further perturbing the membrane structure. This effect was more substantial for the POPS bilayer.

Finally, we simulated the insertion of Pep$_{Mt-II}$ in a membrane composed of 75% POPC and 25% POPS, a composition closer to the complex heterogeneity of eukaryotic cell membranes. This membrane also displayed a significant thinning near Pep$_{Mt-II}$ (Figure 3), whose extent (2.55 nm) was between the values for the pure POPC and POPS membranes (2.85 and 2.43 nm). POPS molecules clustered around Pep$_{Mt-II}$ (Figure 3). We analyzed the interactions of Pep$_{Mt-II}$ with POPS and POPC phospholipids as well as with water molecules (Figure S1). The results show that Pep$_{Mt-II}$ interacts more frequently with POPS than with POPC. This is particularly notable, given that POPS constitutes only 25% of the phospholipids in the simulated membrane, while POPC makes up 75%. Additionally, Pep$_{Mt-II}$ interacts with water molecules along its entire length, with even the most buried residues making contact with water. The Lys and Arg residues, including centrally located Lys, are the most highly solvated. These residues play a crucial role in facilitating water infiltration into the membrane and contributing to membrane destabilization. In summary, even a single, monodispersed snake-venom-derived peptide causes membrane thinning and deep penetration of water molecules.

All-Atom Translocation of Ca^{2+} through Membranes Containing Pep$_{Mt-II}$

The first event observed when PLA_2-like proteins or derived peptides act, triggering cell death, is a massive Ca^{2+} intracellular influx.[16] Therefore, we studied the direct involvement of those peptides in facilitating Ca^{2+} internalization by determining the all-atom potential of mean force (PMF) for translocating one Ca^{2+} ion through pure POPC, pure POPS, and mixed membranes, near Pep$_{Mt-II}$ aggregates of different sizes, and, as a control, in membranes without the peptide.

The two pure bilayers represent extreme conditions, i.e., membrane regions where the negative or zwitterionic phospholipids cluster around Pep$_{Mt-II}$. We did not expect that a lipid mixture would largely alter the conclusions made from the obtained PMFs. Membrane properties for the lipid

https://doi.org/10.1021/jacsau.4c00646
JACS Au 2024, 4, 4295−4306

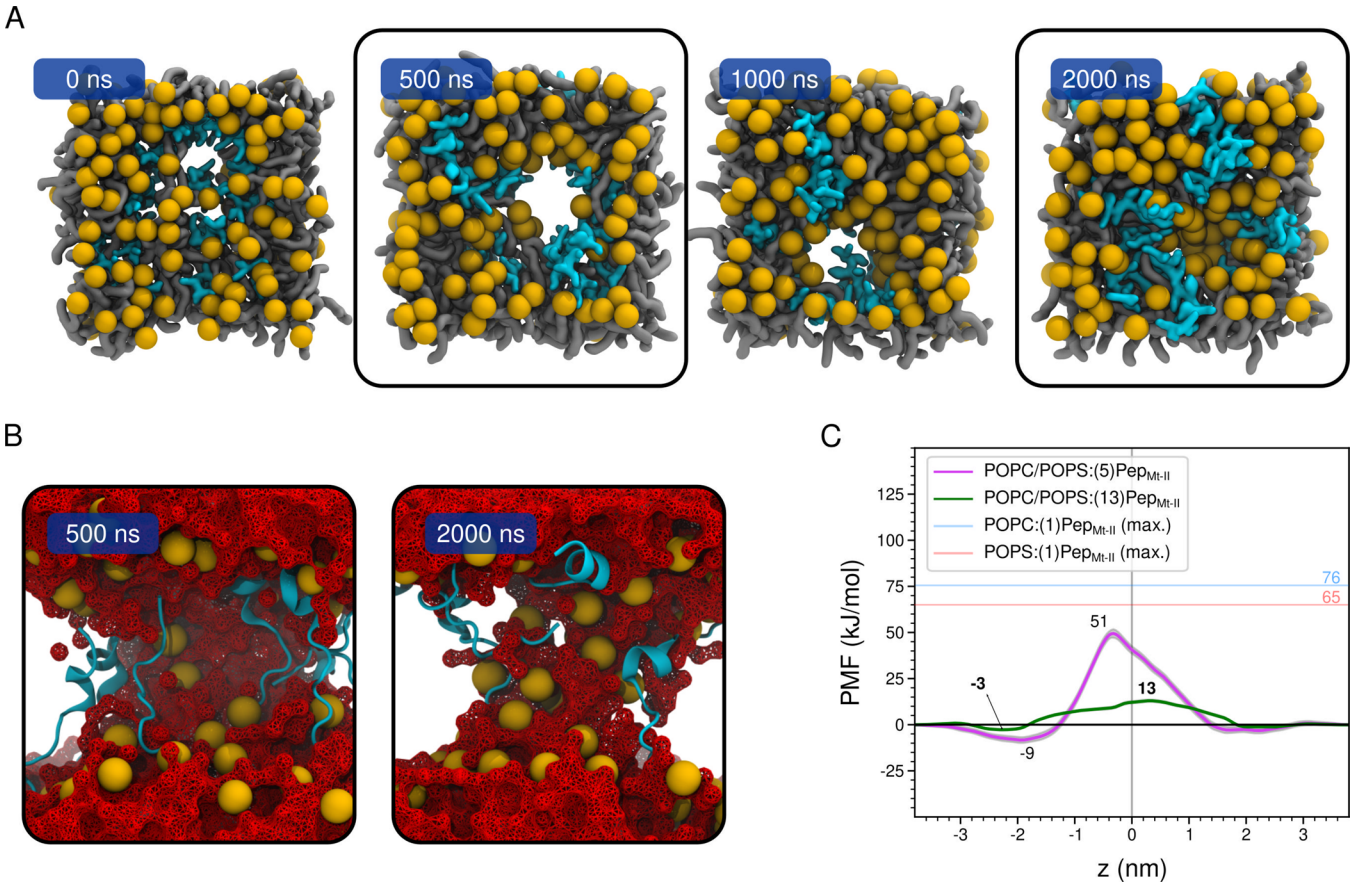

Figure 5. Representative snapshots of the simulations with a lipid-to-peptide ratio of 10:1 and PMFs for Ca^{2+} translocation. (A) Representative snapshots of the simulation, showcasing the P atoms (orange spheres), the lipid tails (gray surface), and the peptide molecules (cyan surface). Water molecules, counterions, and some of the lipid atoms are omitted for clarity. The 0 ns snapshot represents the structure after equilibration. (B) Side-view of the snapshots at 500 ns and at the end of the 2 μs simulation. We showcased the P atoms (orange spheres), the peptide molecules (cyan cartoon), and the water molecules (red mesh). Other molecules were omitted for clarity. (C) PMFs for Ca^{2+} translocation for the system with a lipid-to-peptide ratio of 10:1 at 500 ns (red curve) and for the system with a lipid-to-peptide ratio of 26:1 (magenta curve). The maximum of the PMFs for Ca^{2+} translocation along pure POPC and POPS bilayers with a single inserted Pep_{Mt-II} molecule is also shown (in transparency).

mixture explored here show properties between the two pure bilayer systems (Table S1 and Figure S2).[34−36]

We analyzed three PMF properties: (1) the free energy barrier for crossing the membrane, ΔG_{bar}[37−39]; (2) the difference between the free energy at the minimum and the bulk water region, related to the partition free energy, ΔG_{par}[37,38,40]; (3) the maximum of the PMF, ΔG_{max} (Table 1).

The PMFs showed that a single Pep_{Mt-II} molecule facilitates Ca^{2+} translocation by substantially reducing the free energy barrier of the process (Figure 4). The reduction ranged from 24 to 51 kJ mol^{-1} depending on the lipid composition, being more pronounced for pure POPS, consistent with the membrane perturbations previously discussed. The POPS membrane induced a much larger partition for Ca^{2+} than the POPC membrane, independently of the presence of Pep_{Mt-II} (ΔG_{par} of −29 vs −1 kJ mol^{-1} for the pure systems with Pep_{Mt-II}). The negative headgroups attracted and stabilized Ca^{2+} much more extensively than the zwitterionic ones. The drop in the free energy maximum for Ca^{2+} translocation induced by a single Pep_{Mt-II} molecule was significant (from 120 to 65 kJ mol^{-1} in the POPS system). For the POPC system, the drop was less considerable, at only 20 kJ mol^{-1} (Table 1).

Finally, we calculated the permeability coefficient using the inhomogeneous solubility diffusion model (ISDM) for each situation (Table 1).[41−46] The calculated membrane permeability coefficient (P_m) for Ca^{2+} translocation in the pure POPC system, 7.3×10^{-15} cm s^{-1}, differed only in 1.1 log units from the experimental values using egg PC large unilamellar vesicles (LUVs), 9.8×10^{-14} cm s^{-1}.[47] The P_m for the pure POPS system was smaller than that of POPC, 7.0×10^{-18} cm s^{-1}. Inserting a single Pep_{Mt-II} peptide significantly increases P_m to 6.7×10^{-9} cm s^{-1} in pure POPS and 4.0×10^{-11} cm s^{-1} in pure POPC. However, the P_m values were too small for rapid Ca^{2+} internalization, well below those of substances that quickly cross cell membranes by passive diffusion, such as therapeutic drugs, whose permeability is about 10^{-6} cm s^{-1}.[48−52]

In summary, the resulting free energy profile shows that monodispersed Pep_{Mt-II} peptides were incapable of facilitating Ca^{2+} internalization in a time frame compatible with the onset of the effects of snakebite envenomation or the quick onset of cytotoxicity observed experimentally with the snake venom-derived peptides.

All-Atom Translocation of Ca^{2+} through Membranes Containing Pep_{Mt-II} Aggregates

As a single Pep_{Mt-II} ligand was insufficient to reproduce the experimental rate of Ca^{2+} internalization, we used all-atom simulations to calculate the Ca^{2+} increase in permeability induced by larger Pep_{Mt-II} aggregates, previously observed in

https://doi.org/10.1021/jacsau.4c00646
JACS Au 2024, 4, 4295−4306

the CG MD simulations. Even though we could have backmapped the CG pores, we preferred to generate them through all-atom MD simulation to avoid any slight structural inaccuracy we might inherit from the CG simulations. To overcome the very high computational burden due to the slow diffusion of the initially dispersed peptides toward aggregation, we used a substantial (albeit safely physiological)[53] $Pep_{Mt\text{-}II}$ concentration with five and 13 peptides inserted into the cell membrane model, which resulted in a lipid-to-peptide ratio of ca. 26:1 and 10:1.

A $Pep_{Mt\text{-}II}$ aggregate with 3−4 molecules quickly formed in the system with a lipid-to-peptide ratio of ca. 26:1, provoking a thinning around the peptides more extensive than in the systems with a single peptide (Figure S3). More water molecules penetrated the bilayer hydrophobic region deeply, generating a higher membrane perturbation due to a larger peptide aggregate (Figure S3). However, the peptides did not form barrel staves or toroidal pores within the time scale of all-atom simulations (1 μs). A larger aggregate of peptides with different relative orientations may be required to create the pores.[26,54,55]

The free energy barrier for Ca^{2+} translocation near the 3−4 peptide aggregate was 60 kJ mol^{-1} (Figure 5), lower than those obtained for the pure lipid bilayers with a single inserted peptide, reflecting the higher membrane perturbation and more extensive water penetration caused by $Pep_{Mt\text{-}II}$ aggregation. The local membrane thinning is the lowest so far (Figure S3). Furthermore, the Ca^{2+} permeability increased substantially to 1.3×10^{-6} cm s^{-1} (Table 1). Thus, the peptide aggregate size strongly facilitates the internalization of Ca^{2+}, even without forming a pore, due to the extensive penetration of water molecules into the membrane. In line with this observation, we simulated even larger aggregates by modeling a system with a lipid-to-peptide ratio of 10:1. In this proportion, the peptide concentration remained well within physiological limits.

In the all-atom MD simulation of this last system, a large pore with eight $Pep_{Mt\text{-}II}$ molecules spanning the complete width of the lipid bilayer spontaneously formed, reaching a maximum diameter after ca. 0.5 μs (Figure 5). The other peptide molecules migrated to the pore vicinity, probably also helping to stabilize the pore. After 1 μs of all-atom simulation, the pore reduced in size and shrank. After 2 μs of all-atom simulation, the large pore started to close, although membrane deformation was still evident. At this point, most of the peptides migrate to the surface of both leaflets, reducing membrane tension. However, there was still a high deformation of the lipid and water molecules inside the membrane, with the lipid head groups projected toward the center of the bilayer (Figure S4). Furthermore, we generated contact maps to visualize peptide interactions at different stages of the simulation (Figure S5). These maps suggest that peptide−peptide interactions play a role in stabilizing the pore. However, the evolving nature of these contacts throughout the simulation highlights the transient and disordered nature of the pore structure. In summary, $Pep_{Mt\text{-}II}$ forms transient, disordered pores without the "ideal" barrel stave or toroidal geometries.[53] Pore transiency is commonly observed with membrane-inserting peptides.[56] The behavior observed here agrees with the experimental observation. Shrinkage is likely due to the equilibration of the peptides across the bilayer.[57]

We calculated the PMF for Ca^{2+} translocation by diffusion through a large pore. The process is very fast with a free energy barrier of 16 kJ mol^{-1} and a calculated permeability of 8.9×10^{-1} cm s^{-1}, exceeding that of typical pharmaceutical drugs that enter the cell through passive diffusion. Therefore, the observed large and transient peptide pores finally explain the experimentally observed burst of intracellular Ca^{2+} concentration and cell death caused by the exposure to the viper venom PLA_2 toxins and their derived peptides

CONCLUSIONS

We investigated the molecular origin of the high toxicity of peptides derived from viper venom PLA_2-like proteins. Physiologically, the peptides and their parent toxins cause a burst in intracellular Ca^{2+} that triggers a series of events ultimately leading to cell death. The C-terminal segment of the *B. asper* venom Myotoxin-II, $Pep_{Mt\text{-}II}$, represented the viper venom-derived class of peptides.

CG MD simulations started with $Pep_{Mt\text{-}II}$ peptides at low concentrations dispersed throughout the membrane. Despite this, the peptides spontaneously aggregated and formed $Pep_{Mt\text{-}II}$ aggregates of several sizes.

This phenomenon was studied in detail in all-atom MD simulations. The results showed that even a single $Pep_{Mt\text{-}II}$ peptide induced a significant change in the local membrane properties, with the most obvious being membrane thinning and water protrusion. Larger aggregates of 4−8 $Pep_{Mt\text{-}II}$ molecules formed a pore similar to that in CG MD simulations. The pore achieved a maximum extension at ca. 500 ns, was disordered, did not fall into the ideal barrel stave or toroidal pore geometries, and closed extensively after 2 μs.

The free energy profiles for internalizing Ca^{2+} ions showed barrier heights that decreased with an increasing aggregate size. Consistently, the Ca^{2+} permeability increased with increasing aggregate size. In the larger aggregate tested, which formed a transient pore, the Ca^{2+} ions crossed the membrane with a very low barrier and a permeability higher than pharmaceutical drugs, explaining the molecular origin of snake venom $Pep_{Mt\text{-}II}$ toxicity: the peptides spontaneously aggregate and form water-filled pores on the membrane that act as highways for the (experimentally observed) free flow of extracellular Ca^{2+} into the cell, triggering a series of events leading to cell death.

In vivo envenoming is a very complex phenomenon. Cell membranes are more heterogeneous than the ones we simulated. They have a significant cholesterol content, and one-third of them comprise peripheric and transmembrane proteins. In addition, the membrane potential further facilitates the internalization of Ca^{2+}. However, experimental evidence shows that the PLA_2-like proteins and peptides derived from them can disrupt naked vesicles composed only of phospholipids (in both simple and more complex mixtures).[16,58−61] Therefore, simple membranes are good models for the peptide effect on cell membranes.

The presented mechanism is likely general for many other peptides derived from snake venom PLA_2-like proteins, particularly for those more similar in size, sequence, and amphiphilicity to $Pep_{Mt\text{-}II}$. In the future, simulations with a large variety of peptides can reinforce the generality of the conclusions among snake species. In addition to explaining the molecular origin of the toxicity of a fascinating class of snake venom peptides, this study will contribute to the development of strategies to enhance the antimicrobial, antiviral, and antiparasitic bioactivity of this class of peptides.

https://doi.org/10.1021/jacsau.4c00646
JACS Au 2024, 4, 4295−4306

METHODS

No unexpected or unusually high safety hazards were encountered.

Coarse-Grained Molecular Dynamics (CG MD) Simulations

We prepared the simulation systems with CHARMM-GUI,[62,63] incorporating a lipid bilayer formed of 256 phospholipids. We varied the phospholipid ratio, generating membranes with distinct compositions: (i) 100% POPC, (ii) 15% POPS and 85% POPC, (iii) 30% POPS and 70% POPC, and (iv) 100% POPS. Each system included 12 $Pep_{Mt\text{-}II}$ molecules (lipid-to-peptide ratio of ca. 21) and 0.15 M of ions. Table S2 shows the details of the simulated systems.

The Martini version 2.2 force field was used to describe the CG systems.[64] The equilibration of the systems lasted 500 ns. Then, the $Pep_{Mt\text{-}II}$ molecules were pulled to the membrane using an umbrella potential, and the MD simulations ran during 600 ns. Subsequently, we carried out production simulations with no constraints, a total of 600 ns per system. We avoided membrane buckling by applying a flat-bottomed position restrain in the *z*-direction (perpendicular to the membrane plane) in the glycerol bead of the phospholipid molecules.[65] Further details on the MD simulations are provided in Supporting Information.[66−69]

All-Atom Molecular Dynamics (AA MD) Simulations—Preparation of the Hydrated Bilayer Model Systems

A set of systems where no peptide was added contained 128 phospholipids of two types, POPC and POPS phospholipids, in different proportions. Their composition is described in Table S2 (systems AA-1, AA-2, and AA-5). We generated the membranes with the CHARMM-GUI interface.[70−74] Each lipid was hydrated by 60 water molecules, and the concentration of Na^+ and Cl^- ions was fixed to 0.15 M. In systems containing negatively charged lipids (i.e., POPS), Na^+ ions were also used to neutralize the system's global net charge. The systems were described using the CHARMM36m force field,[75] combined with the TIP3P water model. Equilibration was achieved using an energy minimization and two *NVT*, and five *NPT* equilibration stages (with gradual position and dihedral restraints release). The simulation details can be found in Supporting Information.[32,68,76−83]

All-Atom Molecular Dynamics (AA MD) Simulations—Preparation of the Membrane-Peptide Model Systems

We extracted the structure of the Lys49 PLA_2-like protein (commonly named as Myotoxin-II) from the RCSB Protein Data Bank, PDB ID 1CLP (10.2210/pdb 1CLP/pdb),[84] and only kept the $Pep_{Mt\text{-}II}$ segment, which has the sequence KKYRYYLKPLCKK and residues number p115−129 (standard numbering system).[15] We uploaded $Pep_{Mt\text{-}II}$ to CHARMM-GUI and patched the terminal groups using an acylated N-terminus and a methyl amidated C-terminus. We then integrated it into the different bilayer systems, spanning the bilayer (systems AA-3, AA-4, and AA-6). We did not directly simulate the insertion of the $Pep_{Mt\text{-}II}$ peptide due to the inherent challenges of achieving ergodicity and convergence in such simulations, particularly at high peptide densities. However, experimental data strongly support the peptide's insertion into the membrane. Its length aligns with the bilayer thickness, and the consensus sequence features positively charged residues at both termini, corresponding to the negative phosphate groups when the peptide inserts perpendicularly to the membrane plane. Additionally, its hydrophobic core aligns seamlessly with the lipid tails along its entire length. These structural features, combined with experimental evidence of membrane disruption, underscore that peptide insertion is crucial for its myotoxic effects. The simulation details can be found in Supporting Information.

In system AA-7, which has a high lipid-to-peptide ratio of ca. 26:1, we inserted five $Pep_{Mt\text{-}II}$ molecules in the membrane with the same orientation relative to the bilayer normal. Furthermore, we moved one of the POPS lipids from one leaflet to the other to ensure that both upper and lower leaflet areas were similar. In system AA-8, with an even higher lipid-to-peptide ratio, the $Pep_{Mt\text{-}II}$ molecules were randomly distributed in the bilayer segment perpendicularly using the PACKMOL program.[85] In this case, the number of water molecules was higher (90 water molecules per lipid) to account for the expansion of the bilayer using such a high concentration of peptide. This configuration has a lipid-to-peptide ratio of ca. 10:1. Like in system AA-7, there was an asymmetry in the bilayer composition, in which one of the negatively charged phospholipids was moved from one leaflet to the other.

Calcium Insertion and Umbrella Sampling Simulations

After the equilibration of the systems, we used the last structure as a starting configuration for the subsequent umbrella sampling simulations to determine the free energy profile of Ca^{2+} translocation along the hydrated bilayers, with (systems AA-3, AA-4, AA-7, and AA-8) and without (systems AA-1 and AA-2) $Pep_{Mt\text{-}II}$ molecule(s) inserted in the bilayer. We removed two sodium ions from the equilibrated systems and inserted a single calcium ion along the bilayer's normal with configurations spaced by 0.1 nm. A total of 77 initial configurations were created (umbrella sampling windows) along an axis centered at the middle of the membrane, perpendicular to the bilayer with coordinates spanning from −3.8 to 3.8 nm. Those positions cover a transfer from the bulk water to bulk water across the bilayer. For the systems with a single peptide (AA-3 and AA-4), three different starting configurations were used per system, spanning different initial positions of the calcium ion relative to the $Pep_{Mt\text{-}II}$ to improve the sampling in these systems. For the multipeptide situations (systems AA-7 and AA-8), the calcium was positioned close to a location with a high agglomeration of $Pep_{Mt\text{-}II}$ or where the water pore was larger. After this protocol, we ran 140 ns simulations per umbrella sampling (US) window. Full details of the US simulation are provided in Supporting Information (Figure S6).[86−95]

ASSOCIATED CONTENT

Data Availability Statement

GROMACS input files and the most relevant all-atom output trajectories were made available at the public repository Zenodo, 10.5281/zenodo.11205292. Other MD simulation trajectories and input files generated and/or analyzed during the current study are available from the authors on request. GROMACS is a free and open-source software suite for high-performance molecular dynamics and output analysis (https://www.gromacs.org/). We have used GROMACS 2021.5 version. For molecular visualization and image rendering, we have used Open-Source PyMOL, version 2.3.0 (available at https://github.com/schrodinger/pymol-open-source) and VMD 1.9.4 (available at https://www.ks.uiuc.edu/Research/vmd/). The commercial PyMOL product with maintenance and support is available from https://pymol.org.

Supporting Information

The Supporting Information is available free of charge at https://pubs.acs.org/doi/10.1021/jacsau.4c00646.

Extended computational methods; supporting figures S1−S6; supporting tables S1, S2; and supporting reference list (PDF)

AUTHOR INFORMATION

Corresponding Author

Pedro A. Fernandes − *LAQV, REQUIMTE, Departamento de Química e Bioquímica, Faculdade de Ciências, Universidade do Porto, 4169-007 Porto, Portugal;* orcid.org/0000-0003-2748-4722; Email: pafernan@fc.up.pt

https://doi.org/10.1021/jacsau.4c00646
JACS Au 2024, 4, 4295−4306

Authors

João T. S. Coimbra − *LAQV, REQUIMTE, Departamento de Química e Bioquímica, Faculdade de Ciências, Universidade do Porto, 4169-007 Porto, Portugal;* orcid.org/0000-0001-9138-7498

Antoine Gissler − *LAQV, REQUIMTE, Departamento de Química e Bioquímica, Faculdade de Ciências, Universidade do Porto, 4169-007 Porto, Portugal*

Emiel Nitor − *STRUCCHEM, Department of Chemistry, University of Antwerp, Antwerpen 2020, Belgium;* orcid.org/0009-0002-5751-5227

Kiana Rostamipour − *STRUCCHEM, Department of Chemistry, University of Antwerp, Antwerpen 2020, Belgium*

Ana V. Cunha − *STRUCCHEM, Department of Chemistry, University of Antwerp, Antwerpen 2020, Belgium;* orcid.org/0000-0001-8996-2860

Maria J. Ramos − *LAQV, REQUIMTE, Departamento de Química e Bioquímica, Faculdade de Ciências, Universidade do Porto, 4169-007 Porto, Portugal;* orcid.org/0000-0002-7554-8324

Complete contact information is available at: https://pubs.acs.org/10.1021/jacsau.4c00646

Author Contributions

The manuscript was written through contributions of all authors. All authors have given approval to the final version of the manuscript. J.T.S.C., A.G., A.V.C., M.J.R., and P.A.F. designed the research; J.T.S.C. and A.G. performed and analyzed the all-atom simulations; E.N., K.R., and A.V.C. performed and analyzed the coarse-grained simulations; J.T.S.C., A.G., A.V.C., M.J.R., and P.A.F. wrote the paper. CRediT: **João T. S. Coimbra** conceptualization, formal analysis, investigation, methodology, supervision, validation, visualization, writing - original draft, writing - review & editing; **Antoine Gissler** conceptualization, formal analysis, investigation, methodology, software, visualization, writing - original draft, writing - review & editing; **Emiel Nitor** formal analysis, investigation, methodology, visualization; **Kiana Rostamipour** formal analysis, investigation, methodology, validation; **Ana V. Cunha** conceptualization, formal analysis, investigation, methodology, resources, supervision, validation, visualization, writing - original draft, writing - review & editing; **Maria João Ramos** funding acquisition, resources, supervision, writing - review & editing; **Pedro Alexandrino Fernandes** conceptualization, funding acquisition, project administration, resources, supervision, writing - review & editing.

Funding

This work received financial support from FCT/MCTES (UIDB/50006/2020 DOI 10.54499/UIDB/50006/2020) through national funds.

Notes

The authors declare no competing financial interest.

■ ACKNOWLEDGMENTS

This work received support and help from national funds (FCT/MCTES, *Fundação para a Ciência e Tecnologia* and *Ministério da Ciência, Tecnologia e Ensino Superior*) through projects: LA/P/0008/2020 DOI 10.54499/LA/P/0008/2020, UIDP/50006/2020 DOI 10.54499/UIDP/50006/2020, and UIDB/50006/2020 DOI 10.54499/UIDB/50006/2020. This work received financial support from National Funds (FCT) through project PTDC/QUI-OUT/1401/2020. This work was produced with the support of the High Performance Computing at the University of Évora (HPCUÉ) and it was funded by FCT I.P. under the project Advanced Computing Project 2021.09753.CPCA.A2, platform Oblivion. The authors gratefully acknowledge the HPC RIVR consortium (www.hpc-rivr.si) and EuroHPC JU (eurohpc-ju.europa.eu) for funding this research by providing computing resources of the HPC system Vega at the Institute of Information Science (www.izum.si). We thank the Centre for Information Technology of the University of Groningen for their support and for providing access to the Peregrine and Hábrók high performance computing clusters. This work also made use of the Dutch national e-infrastructure with the support of the SURF cooperative using grants no. EINF-3817 and NWO-2022.004/L1. J.T.S.C. thanks FCT for funding through the Scientific Employment Stimulus−Individual Call (ref. CEECIND/01374/2018/CP1545/CT0003 DOI 10.54499/CEECIND/01374/2018/CP1545/CT0003). We thank the team of the High-Performance Computing Centre of the University of Évora and Óscar Passos for technical assistance.

■ REFERENCES

(1) Gutiérrez, J. M.; Calvete, J. J.; Habib, A. G.; Harrison, R. A.; Williams, D. J.; Warrell, D. A. Snakebite envenoming. *Nat. Rev. Dis. Primers* **2017**, *3*, 17063.

(2) Oliveira, A. L.; Viegas, M. F.; da Silva, S. L.; Soares, A. M.; Ramos, M. J.; Fernandes, P. A. The chemistry of snake venom and its medicinal potential. *Nat. Rev. Chem.* **2022**, *6*, 451−469.

(3) Williams, D. J.; Abul Faiz, M.; Abela-Ridder, B.; Ainsworth, S.; Bulfone, T. C.; Nickerson, A. D.; Habib, A. G.; Junghanss, T.; Fan, H. W.; Turner, M.; et al. Strategy for a globally coordinated response to a priority neglected tropical disease: Snakebite envenoming. *PLoS Negl. Trop. Dis.* **2019**, *13*, No. e0007059.

(4) Tasoulis, T.; Isbister, G. K. A Review and Database of Snake Venom Proteomes. *Toxins* **2017**, *9*, 290.

(5) Lomonte, B.; Fernández, J. Solving the microheterogeneity of myotoxin-II by high-resolution mass spectrometry: Insights into C-terminal region variability in Lys49-phospholipase A_2 homologs. *Toxicon* **2022**, *210*, 123−131.

(6) Cintra-Francischinelli, M.; Pizzo, P.; Rodrigues-Simioni, L.; Ponce-Soto, L. A.; Rossetto, O.; Lomonte, B.; Gutiérrez, J. M.; Pozzan, T.; Montecucco, C. Calcium imaging of muscle cells treated with snake myotoxins reveals toxin synergism and presence of acceptors. *Cell. Mol. Life Sci.* **2009**, *66*, 1718−1728.

(7) Fernández, J.; Caccin, P.; Koster, G.; Lomonte, B.; Gutiérrez, J. M.; Montecucco, C.; Postle, A. D. Muscle phospholipid hydrolysis by *Bothrops asper* Asp49 and Lys49 phospholipase A_2 myotoxins - distinct mechanisms of action. *Febs J.* **2013**, *280*, 3878−3886.

(8) Dennis, E. A.; Cao, J.; Hsu, Y. H.; Magrioti, V.; Kokotos, G. Phospholipase A_2 Enzymes: Physical Structure, Biological Function, Disease Implication, Chemical Inhibition, and Therapeutic Intervention. *Chem. Rev.* **2011**, *111*, 6130−6185.

(9) Castro-Amorim, J.; de Oliveira, A. N.; Da Silva, S. L.; Soares, A. M.; Mukherjee, A. K.; Ramos, M. J.; Fernandes, P. A. Catalytically Active Snake Venom PLA_2 Enzymes: An Overview of Its Elusive Mechanisms of Reaction. *J. Med. Chem.* **2023**, *66*, 5364−5376.

(10) Maraganore, J. M.; Merutka, G.; Cho, W.; Welches, W.; Kezdy, F. J.; Heinrikson, R. L. A New Class of Phospholipases-A_2 with Lysine in Place of Aspartate 49. Functional Consequences for Calcium and Substrate Binding. *J. Biol. Chem.* **1984**, *259*, 13839−13843.

(11) Incerpi, S.; Devito, P.; Luly, P.; Rufini, S. Effect of Ammodytin-L from Vipera-Ammodytes on L-6 Cells from Rat Skeletal-Muscle. *Biochim. Biophys. Acta, Mol. Cell Res.* **1995**, *1268*, 137−142.

(12) Villalobos, J. C.; Mora, R.; Lomonte, B.; Gutierrez, J. M.; Angulo, Y. Cytotoxicity induced in myotubes by a Lys49 phospholipase A_2 homologue from the venom of the snake: Evidence

of rapid plasma membrane damage and a dual role for extracellular calcium. *Toxicol in Vitro* **2007**, *21*, 1382−1389.
(13) Gutierrez, J. M.; Chaves, F.; Gene, J. A.; Lomonte, B.; Camacho, Z.; Schosinsky, K. Myonecrosis Induced in Mice by a Basic Myotoxin Isolated from the Venom of the Snake *Bothrops nummifer* (Jumping Viper) from Costa-Rica. *Toxicon* **1989**, *27*, 735−745.
(14) Cintra-Francischinelli, M.; Caccin, P.; Chiavegato, A.; Pizzo, P.; Carmignoto, G.; Angulo, Y.; Lomonte, B.; Gutiérrez, J. M.; Montecuccoa, C. Bothrops snake myotoxins induce a large efflux of ATP and potassium with spreading of cell damage and pain. *Proc. Natl. Acad. Sci. U. S. A.* **2010**, *107*, 14140−14145.
(15) Renetseder, R.; Brunie, S.; Dijkstra, B. W.; Drenth, J.; Sigler, P. B. A Comparison of the Crystal-Structures of Phospholipase-A_2 from Bovine Pancreas and *Crotalus atrox* Venom. *J. Biol. Chem.* **1985**, *260*, 11627−11634.
(16) Lomonte, B. Lys49 myotoxins, secreted phospholipase A_2-like proteins of viperid venoms: A comprehensive review. *Toxicon* **2023**, *224*, No. 107024.
(17) Cintra-Francischinelli, M.; Pizzo, P.; Angulo, Y.; Gutiérrez, J. M.; Montecucco, C.; Lomonte, B. The C-terminal region of a Lys49 myotoxin mediates Ca^{2+} influx in C2C12 myotubes. *Toxicon* **2010**, *55*, 590−596.
(18) Lomonte, B.; Moreno, E.; Tarkowski, A.; Hanson, L. A.; Maccarana, M. Neutralizing Interaction between Heparins and Myotoxin-II, a Lysine 49 Phospholipase A_2 from *Bothrops asper* Snake Venom. Identification of a Heparin-Binding and Cytolytic Toxin Region by the Use of Synthetic Peptides and Molecular Modeling. *J. Biol. Chem.* **1994**, *269*, 29867−29873.
(19) Lomonte, B.; Angulo, Y.; Moreno, E. Synthetic Peptides Derived from the C-Terminal Region of Lys49 Phospholipase A_2 Homologues from Viperidae Snake Venoms: Biomimetic Activities and Potential Applications. *Curr. Pharm. Design* **2010**, *16*, 3224−3230.
(20) Moretta, A.; Scieuzo, C.; Petrone, A. M.; Salvia, R.; Manniello, M. D.; Franco, A.; Lucchetti, D.; Vassallo, A.; Vogel, H.; Sgambato, A.; et al. Antimicrobial Peptides: A New Hope in Biomedical and Pharmaceutical Fields. *Front Cell Infect Mi* **2021**, *11*, No. 668632.
(21) Alape-Girón, A.; Sanz, L.; Escolano, J.; Flores-Díaz, M.; Madrigal, M.; Sasa, M.; Calvete, J. J. Snake venomics of the lancehead pitviper *Bothrops asper*: geographic, individual, and ontogenetic variations. *J. Proteome Res.* **2008**, *7*, 3556−3571.
(22) Sasa, M.; Wasko, D. K.; Lamar, W. W. Natural history of the terciopelo *Bothrops asper* (Serpentes: Viperidae) in Costa Rica. *Toxicon* **2009**, *54*, 904−922.
(23) Lomonte, B.; Angulo, Y.; Santamaría, C. Comparative study of synthetic peptides corresponding to region 115−129 in Lys49 myotoxic phospholipases A_2 from snake venoms. *Toxicon* **2003**, *42*, 307−312.
(24) de Oliveira, A. L. N.; Lacerda, M. T.; Ramos, M. J.; Fernandes, P. A. Viper Venom Phospholipase A2 Database: The Structural and Functional Anatomy of a Primary Toxin in Envenomation. *Toxins* **2024**, *16*, 71.
(25) Almeida, J. R.; Mendes, B.; Lancellotti, M.; Marangoni, S.; Vale, N.; Passos, O.; Ramos, M. J.; Fernandes, P. A.; Gomes, P.; Da Silva, S. L. A novel synthetic peptide inspired on Lys49 phospholipase A_2 from *Crotalus oreganus abyssus* snake venom active against multidrug-resistant clinical isolates. *Eur. J. Med. Chem.* **2018**, *149*, 248−256.
(26) Tuerkova, A.; Kabelka, I.; Králová, T.; Sukeník, L.; Pokorná, S.; Hof, M.; Vácha, R. Effect of helical kink in antimicrobial peptides on membrane pore formation. *eLife* **2020**, *9*, No. e47946.
(27) Nguyen, L. T.; Haney, E. F.; Vogel, H. J. The expanding scope of antimicrobial peptide structures and their modes of action. *Trends Biotechnol* **2011**, *29*, 464−472.
(28) Bernardes, C. E. S. AGGREGATES: Finding Structures in Simulation Results of Solutions. *J. Comput. Chem.* **2017**, *38*, 753−765.
(29) Sengupta, D.; Leontiadou, H.; Mark, A. E.; Marrink, S. J. Toroidal pores formed by antimicrobial peptides show significant disorder. *Bba-Biomembranes* **2008**, *1778*, 2308−2317.
(30) de Oliveira, A. H. C.; Ferreira, T. L.; Ward, R. J. Reduced pH induces an inactive non-native conformation of the monomeric bothropstoxin-I (Lys49-PLA_2). *Toxicon* **2009**, *54*, 373−378.
(31) Franco, L. R.; Park, P.; Chaimovich, H.; Coutinho, K.; Cuccovia, I. M.; Lima, F. S. Simulations reveal that antimicrobial BP100 induces local membrane thinning, slows lipid dynamics and favors water penetration. *Rsc Adv.* **2022**, *12*, 4573−4588.
(32) Gapsys, V.; de Groot, B. L.; Briones, R. Computational analysis of local membrane properties. *J. Comput. Aid Mol. Des* **2013**, *27*, 845−858.
(33) Neale, C.; Hsu, J. C. Y.; Yip, C. M.; Pomès, R. Indolicidin Binding Induces Thinning of a Lipid Bilayer. *Biophys. J.* **2014**, *106*, L29−L31.
(34) Kucerka, N.; Nieh, M. P.; Katsaras, J. Fluid phase lipid areas and bilayer thicknesses of commonly used phosphatidylcholines as a function of temperature. *Bba-Biomembranes* **2011**, *1808*, 2761−2771.
(35) Kucerka, N.; Tristram-Nagle, S.; Nagle, J. F. Structure of fully hydrated fluid phase lipid bilayers with monounsaturated chains. *J. Membr. Biol.* **2006**, *208*, 193−202.
(36) Pan, J. J.; Cheng, X. L.; Monticelli, L.; Heberle, F. A.; Kucerka, N.; Tieleman, D. P.; Katsaras, J. The molecular structure of a phosphatidylserine bilayer determined by scattering and molecular dynamics simulations. *Soft Matter* **2014**, *10*, 3716−3725.
(37) Jin, T. Y.; Patel, S. J.; Van Lehn, R. C. Molecular simulations of lipid membrane partitioning and translocation by bacterial quorum sensing modulators. *PLoS One* **2021**, *16*, No. e0246187.
(38) Paloncyová, M.; Fabre, G.; DeVane, R. H.; Trouillas, P.; Berka, K.; Otyepka, M. Benchmarking of Force Fields for Molecule-Membrane Interactions. *J. Chem. Theory Comput* **2014**, *10*, 4143−4151.
(39) Sugita, M.; Fujie, T.; Yanagisawa, K.; Ohue, M.; Akiyama, Y. Lipid Composition Is Critical for Accurate Membrane Permeability Prediction of Cyclic Peptides by Molecular Dynamics Simulations. *J. Chem. Inf Model* **2022**, *62*, 4549−4560.
(40) Magalhaes, P. R.; Reis, P. B. P. S.; Vila-Viçosa, D.; Machuqueiro, M.; Victor, B. L. Optimization of an *in silico* Protocol Using Probe Permeabilities to Identify Membrane Pan-Assay Interference Compounds. *J. Chem. Inf. Model.* **2022**, *62*, 3034−3042.
(41) Marrink, S. J.; Berendsen, H. J. C. Simulation of Water Transport through a Lipid-Membrane. *J. Phys. Chem-Us* **1994**, *98*, 4155−4168.
(42) Gaalswyk, K.; Awoonor-Williams, E.; Rowley, C. N. Generalized Langevin Methods for Calculating Transmembrane Diffusivity. *J. Chem. Theory Comput* **2016**, *12*, 5609−5619.
(43) Awoonor-Williams, E.; Rowley, C. N. Molecular simulation of nonfacilitated membrane permeation. *Bba-Biomembranes* **2016**, *1858*, 1672−1687.
(44) Lee, C. T.; Comer, J.; Herndon, C.; Leung, N.; Pavlova, A.; Swift, R. V.; Tung, C.; Rowley, C. N.; Amaro, R. E.; Chipot, C.; et al. Simulation-Based Approaches for Determining Membrane Permeability of Small Compounds. *J. Chem. Inf Model* **2016**, *56*, 721−733.
(45) Coimbra, J. T. S.; Feghali, R.; Ribeiro, R. P.; Ramos, M. J.; Fernandes, P. A. The importance of intramolecular hydrogen bonds on the translocation of the small drug piracetam through a lipid bilayer. *Rsc Adv.* **2021**, *11*, 899−908.
(46) Filipe, H. A. L.; Javanainen, M.; Salvador, A.; Galvao, A. M.; Vattulainen, I.; Loura, L. M. S.; Moreno, M. J. Quantitative Assessment of Methods Used To Obtain Rate Constants from Molecular Dynamics Simulations-Translocation of Cholesterol across Lipid Bilayers. *J. Chem. Theory Comput* **2018**, *14*, 3840−3848.
(47) Zeng, J. W.; Borchman, D.; Paterson, C. A. Calcium permeability in large unilamellar vesicles prepared from bovine lens cortical lipids. *Exp. Eye Res.* **1997**, *64*, 115−120.
(48) Shinoda, W.; Mikami, M.; Baba, T.; Hato, M. Molecular dynamics study on the effects of chain branching on the physical properties of lipid bilayers: 2. *Permeability. J. Phys. Chem. B* **2004**, *108*, 9346−9356.

https://doi.org/10.1021/jacsau.4c00646
JACS Au 2024, 4, 4295−4306

(49) Bemporad, D.; Essex, J. W.; Luttmann, C. Permeation of small molecules through a lipid bilayer: A computer simulation study. *J. Phys. Chem. B* **2004**, *108*, 4875−4884.
(50) Vorobyov, I.; Olson, T. E.; Kim, J. H.; Koeppe, R. E.; Andersen, O. S.; Allen, T. W. Ion-Induced Defect Permeation of Lipid Membranes. *Biophys. J.* **2014**, *106*, 586−597.
(51) Frallicciardi, J.; Melcr, J.; Siginou, P.; Marrink, S. J.; Poolman, B. Membrane thickness, lipid phase and sterol type are determining factors in the permeability of membranes to small solutes. *Nat. Commun.* **2022**, *13*, 1605.
(52) O'Hagan, S.; Kell, D. B. The apparent permeabilities of Caco-2 cells to marketed drugs: magnitude, and independence from both biophysical properties and endogenite similarities. *Peerj* **2015**, *3*, No. e1405.
(53) Melo, M. N.; Ferre, R.; Castanho, M. A. R. B. OPINION Antimicrobial peptides: linking partition, activity and high membrane-bound concentrations. *Nature Reviews Microbiology* **2009**, *7*, 245−250.
(54) Strandberg, E.; Bentz, D.; Wadhwani, P.; Bürck, J.; Ulrich, A. S. Terminal charges modulate the pore forming activity of cationic amphipathic helices. *Bba-Biomembranes* **2020**, *1862*, No. 183243.
(55) Strandberg, E.; Bentz, D.; Wadhwani, P.; Ulrich, A. S. Chiral supramolecular architecture of stable transmembrane pores formed by an α-helical antibiotic peptide in the presence of lysolipids. *Sci. Rep.* **2020**, *10*, 4710.
(56) Kumar, P.; Kizhakkedathu, J. N.; Straus, S. K. Antimicrobial Peptides: Diversity, Mechanism of Action and Strategies to Improve the Activity and Biocompatibility *In Vivo*. *Biomolecules* **2018**, *8*, 4.
(57) Fuertes, G.; Giménez, D.; Esteban-Martín, S.; Sánchez-Muñoz, O. L.; Salgado, J. A lipocentric view of peptide-induced pores. *Eur. Biophys J. Biophy* **2011**, *40*, 399−415.
(58) Pedersen, J. Z.; Dearcuri, B. F.; Morero, R. D.; Rufini, S. Phospholipase-Like Myotoxins Induce Rapid Membrane Leakage of Nonhydrolyzable Ether-Lipid Liposomes. *Bba-Biomembranes* **1994**, *1190*, 177−180.
(59) Ferreira, T. L.; Ward, R. J. The interaction of bothropstoxin-I (Lys49-PLA$_2$) with liposome membranes. *Toxicon* **2009**, *54*, 525−530.
(60) de Oliveira, A. H. C.; Giglio, J. R.; Andriao-Escarso, S. H.; Ito, A. S.; Ward, R. J. A pH-induced dissociation of the dimeric form of a lysine 49-phospholipase A$_2$ abolishes Ca^{2+}-independent membrane damaging activity. *Biochemistry-Us* **2001**, *40*, 6912−6920.
(61) Won, A.; Ianoul, A. Interactions of antimicrobial peptide from C-terminus of myotoxin II with phospholipid mono- and bilayers. *Bba-Biomembranes* **2009**, *1788*, 2277−2283.
(62) Jo, S.; Kim, T.; Iyer, V. G.; Im, W. CHARMM-GUI: a web-based graphical user interface for CHARMM. *J. Comput. Chem.* **2008**, *29*, 1859−1865.
(63) Qi, Y. F.; Ingólfsson, H. I.; Cheng, X.; Lee, J.; Marrink, S. J.; Im, W. CHARMM-GUI Martini Maker for Coarse-Grained Simulations with the Martini Force Field. *J. Chem. Theory Comput* **2015**, *11*, 4486−4494.
(64) de Jong, D. H.; Singh, G.; Bennett, W. F. D.; Arnarez, C.; Wassenaar, T. A.; Schäfer, L. V.; Periole, X.; Tieleman, D. P.; Marrink, S. J. Improved Parameters for the Martini Coarse-Grained Protein Force Field. *J. Chem. Theory Comput* **2013**, *9*, 687−697.
(65) Su, J. J.; Marrink, S. J.; Melo, M. N. Localization Preference of Antimicrobial Peptides on Liquid-Disordered Membrane Domains. *Front. Cell. Dev. Biol.* **2020**, *8*, 350.
(66) Pettersen, E. F.; Goddard, T. D.; Huang, C. C.; Couch, G. S.; Greenblatt, D. M.; Meng, E. C.; Ferrin, T. E. UCSF chimera - A visualization system for exploratory research and analysis. *J. Comput. Chem.* **2004**, *25*, 1605−1612.
(67) Bannwarth, C.; Caldeweyher, E.; Ehlert, S.; Hansen, A.; Pracht, P.; Seibert, J.; Spicher, S.; Grimme, S. Extended tight-binding quantum chemistry methods. *Wiley Interdiscip. Rev.: Comput. Mol. Sci.* **2021**, *11*, No. e1493.
(68) Berendsen, H. J. C.; Postma, J. P. M.; Vangunsteren, W. F.; Dinola, A.; Haak, J. R. Molecular-Dynamics with Coupling to an External Bath. *J. Chem. Phys.* **1984**, *81*, 3684−3690.
(69) Bussi, G.; Donadio, D.; Parrinello, M. Canonical sampling through velocity rescaling. *J. Chem. Phys.* **2007**, *126*, No. 014101.
(70) Kumar, R.; Iyer, V. G.; Im, W. CHARMM-GUI: A graphical user interface for the CHARMM users. *Abstr. Pap. Am. Chem. S* **2007**, *233*, 273−273.
(71) Jo, S.; Kim, T.; Im, W. Automated Builder and Database of Protein/Membrane Complexes for Molecular Dynamics Simulations. *PLoS One* **2007**, *2*, No. e880.
(72) Jo, S.; Lim, J. B.; Klauda, J. B.; Im, W. CHARMM-GUI Membrane Builder for Mixed Bilayers and Its Application to Yeast Membranes. *Biophys. J.* **2009**, *97*, 50−58.
(73) Wu, E. L.; Cheng, X.; Jo, S.; Rui, H.; Song, K. C.; Dávila-Contreras, E. M.; Qi, Y. F.; Lee, J. M.; Monje-Galvan, V.; Venable, R. M.; et al. CHARMM-GUI Membrane Builder Toward Realistic Biological Membrane Simulations. *J. Comput. Chem.* **2014**, *35*, 1997−2004.
(74) Lee, J.; Cheng, X.; Swails, J. M.; Yeom, M. S.; Eastman, P. K.; Lemkul, J. A.; Wei, S.; Buckner, J.; Jeong, J. C.; Qi, Y. F.; et al. CHARMM-GUI Input Generator for NAMD, GROMACS, AMBER, OpenMM, and CHARMM/OpenMM Simulations Using the CHARMM36 Additive Force Field. *J. Chem. Theory Comput* **2016**, *12*, 405−413.
(75) Klauda, J. B.; Venable, R. M.; Freites, J. A.; O'Connor, J. W.; Tobias, D. J.; Mondragon-Ramirez, C.; Vorobyov, I.; MacKerell, A. D.; Pastor, R. W. Update of the CHARMM All-Atom Additive Force Field for Lipids: Validation on Six Lipid Types. *J. Phys. Chem. B* **2010**, *114*, 7830−7843.
(76) Nose, S. A Molecular-Dynamics Method for Simulations in the Canonical Ensemble. *Mol. Phys.* **1984**, *52*, 255−268.
(77) Hoover, W. G. Canonical Dynamics - Equilibrium Phase-Space Distributions. *Phys. Rev. A* **1985**, *31*, 1695−1697.
(78) Parrinello, M.; Rahman, A. Polymorphic Transitions in Single-Crystals - a New Molecular-Dynamics Method. *J. Appl. Phys.* **1981**, *52*, 7182−7190.
(79) Nose, S.; Klein, M. L. Constant Pressure Molecular-Dynamics for Molecular-Systems. *Mol. Phys.* **1983**, *50*, 1055−1076.
(80) Essmann, U.; Perera, L.; Berkowitz, M. L.; Darden, T.; Lee, H.; Pedersen, L. G. A Smooth Particle Mesh Ewald Method. *J. Chem. Phys.* **1995**, *103*, 8577−8593.
(81) Hess, B.; Bekker, H.; Berendsen, H. J. C.; Fraaije, J. G. E. M. LINCS: A linear constraint solver for molecular simulations. *J. Comput. Chem.* **1997**, *18*, 1463−1472.
(82) *The PyMOL Molecular Graphics System, Version 2.3.0*; Schrödinger, LLC: 2019.
(83) Humphrey, W.; Dalke, A.; Schulten, K. VMD: Visual molecular dynamics. *J. Mol. Graph Model* **1996**, *14*, 33−38.
(84) Arni, R. K.; Ward, R. J.; Gutierrez, J. M.; Tulinsky, A. Structure of a Calcium-Independent Phospholipase-Like Myotoxic Protein from *Bothrops asper* Venom. *Acta Crystallogr. D* **1995**, *51*, 311−317.
(85) Martínez, L.; Andrade, R.; Birgin, E. G.; Martínez, J. M. PACKMOL: A Package for Building Initial Configurations for Molecular Dynamics Simulations. *J. Comput. Chem.* **2009**, *30*, 2157−2164.
(86) Jämbeck, J. P. M.; Lyubartsev, A. P. Implicit inclusion of atomic polarization in modeling of partitioning between water and lipid bilayers. *Phys. Chem. Chem. Phys.* **2013**, *15*, 4677−4686.
(87) Kumar, S.; Bouzida, D.; Swendsen, R. H.; Kollman, P. A.; Rosenberg, J. M. The Weighted Histogram Analysis Method for Free-Energy Calculations on Biomolecules 0.1. The Method. *J. Comput. Chem.* **1992**, *13*, 1011−1021.
(88) Berendsen, H. J. C.; Vanderspoel, D.; Vandrunen, R. Gromacs - a Message-Passing Parallel Molecular-Dynamics Implementation. *Comput. Phys. Commun.* **1995**, *91*, 43−56.
(89) Lindahl, E.; Hess, B.; van der Spoel, D. GROMACS 3.0: a package for molecular simulation and trajectory analysis. *J. Mol. Model* **2001**, *7*, 306−317.
(90) Van der Spoel, D.; Lindahl, E.; Hess, B.; Groenhof, G.; Mark, A. E.; Berendsen, H. J. C. GROMACS: Fast, flexible, and free. *J. Comput. Chem.* **2005**, *26*, 1701−1718.

https://doi.org/10.1021/jacsau.4c00646
JACS Au 2024, 4, 4295−4306

(91) Hess, B.; Kutzner, C.; van der Spoel, D.; Lindahl, E. GROMACS 4: Algorithms for highly efficient, load-balanced, and scalable molecular simulation. *J. Chem. Theory Comput* **2008**, *4*, 435−447.
(92) Pronk, S.; Páll, S.; Schulz, R.; Larsson, P.; Bjelkmar, P.; Apostolov, R.; Shirts, M. R.; Smith, J. C.; Kasson, P. M.; van der Spoel, D.; et al. GROMACS 4.5: a high-throughput and highly parallel open source molecular simulation toolkit. *Bioinformatics* **2013**, *29*, 845−854.
(93) Páll, S.; Abraham, M. J.; Kutzner, C.; Hess, B.; Lindahl, E. Tackling Exascale Software Challenges in Molecular Dynamics Simulations with GROMACS. *Lect Notes Comput. Sc* **2015**, *8759*, 3−27.
(94) Abraham, M. J.; Murtola, T.; Schulz, R.; Páll, S.; Smith, J. C.; Hess, B.; Lindahl, E. GROMACS: High performance molecular simulations through multi-level parallelism from laptops to supercomputers. *SoftwareX* **2015**, *1−2*, 19−25.
(95) Pokhrel, N.; Maibaum, L. Free Energy Calculations of Membrane Permeation: Challenges Due to Strong Headgroup-Solute Interactions. *J. Chem. Theory Comput* **2018**, *14*, 1762−1771.

https://doi.org/10.1021/jacsau.4c00646
JACS Au 2024, 4, 4295−4306